

## Hydrogen-induced modification of the electronic structure and magnetic states in Fe, Co, and Ni monohydrides

N. Ishimatsu,<sup>1,\*</sup> T. Shichijo,<sup>1</sup> Y. Matsushima,<sup>1</sup> H. Maruyama,<sup>1</sup> Y. Matsuura,<sup>2</sup> T. Tsumuraya,<sup>3</sup> T. Shishidou,<sup>2</sup> T. Oguchi,<sup>4</sup> N. Kawamura,<sup>5</sup> M. Mizumaki,<sup>5</sup> T. Matsuoka,<sup>6</sup> and K. Takemura<sup>7</sup>

<sup>1</sup>*Department of Physics, Graduate School of Science, Hiroshima University, 1-3-1 Kagamiyama, Higashihiroshima, Hiroshima 739-8526, Japan*

<sup>2</sup>*Graduate School of Advanced Sciences of Matter (ADSM), Hiroshima University, 1-3-1 Kagamiyama, Higashihiroshima, Hiroshima 739-8530, Japan*

<sup>3</sup>*RIKEN Advanced Science Institute, 2-1 Hirosawa, Wako, Saitama 351-0198, Japan*

<sup>4</sup>*The Institute of Scientific and Industrial Research (ISIR), Osaka University, 8-1 Mihogaoka, Ibaraki, Osaka 567-0047, Japan*

<sup>5</sup>*Japan Synchrotron Radiation Research Institute (JASRI), SPring-8, 1-1-1 Kouto, Sayo-cho, Sayo-gun, Hyogo 679-5198, Japan*

<sup>6</sup>*KYOKUGEN, Center for Quantum Science and Technology under Extreme Conditions, Osaka University, Osaka 560-8531, Japan*

<sup>7</sup>*National Institute for Materials Science (NIMS), 1-1 Namiki, Tsukuba, Ibaraki 305-0044, Japan*

(Received 30 December 2011; revised manuscript received 24 August 2012; published 24 September 2012)

Hydrogen-induced modification of electronic structures, magnetic states, and crystal structures of transition metal (TM = Fe, Co, and Ni) monohydrides was investigated using TM  $K$ -edge x-ray magnetic circular dichroism (XMCD), x-ray diffraction, and first-principles calculations. The TM hydrides undergo narrowing of TM  $3d$  density of states (DOS) and significant shifts in the Fermi energy  $E_F$  due to hydrogenation, which is responsible for the magnetic properties of the TM hydrides: ferromagnetic FeH, ferromagnetic CoH, and paramagnetic NiH. The reconstruction of the electronic structure is mainly attributed to the appearance of bonding and antibonding states together with hydrogen-induced volume expansion. We demonstrate that the characteristic XMCD profile of the TM hydrides near the absorption edge probed the reconstruction of the electronic structure above  $E_F$ . The pressure dependence of XMCD revealed that the ferromagnetic state of FeH is less stable than that of CoH under pressure. The different hydrogenation processes between CoH and NiH at room temperature are reported by means of x-ray diffraction.

DOI: [10.1103/PhysRevB.86.104430](https://doi.org/10.1103/PhysRevB.86.104430)

PACS number(s): 71.20.Be, 78.70.Dm, 88.30.rd, 62.50.-p

### I. INTRODUCTION

The interaction between hydrogen and host metals has been of great interest because hydrogenation gives rise to considerable modification of the host metals' physical properties such as crystal structure, electric resistivity, optical transparency, and magnetism.<sup>1,2</sup> In the case of ferromagnetic materials, the Curie temperature and magnetization are modified by even a small amount of hydrogen.<sup>3,4</sup> This implies that magnetic state depends on the reconstruction of the electronic structure due to hydrogenation; in particular, alternation of the electronic structure near the Fermi energy ( $E_F$ ) is a key issue. Because of the simplicity of their crystal structures and the drastic changes in their magnetic properties, hydrogenation of ferromagnetic elements such as Fe, Co, and Ni is the most fundamental model for obtaining a deep understanding of the effects of hydrogen on magnetism and electronic structure.

The transition metal (TM) monohydrides, FeH, CoH, and NiH can be synthesized by a direct reaction with  $H_2$  fluid under gigapascal pressures.<sup>5,6</sup> These TM monohydrides are stable only under high pressure. The crystal structures of the TM hydrides are illustrated in Fig. 1. TM atoms form double hcp (dhcp), hcp, and fcc lattices, and hydrogen atoms occupy their interstitial sites. FeH is synthesized at hydrogen pressure  $p_{H_2} \approx 3.5$  GPa,<sup>7</sup> and the hydride is ferromagnetic at room temperature (RT).<sup>8-10</sup> Because the Fe lattice forms a dhcp structure in FeH,<sup>11</sup> the appearance of the ferromagnetic state is in marked contrast to the paramagnetic state of hcp-Fe high pressure phase.<sup>12</sup> At higher pressures, the eventual loss of fer-

romagnetism in FeH was reported at  $p_{H_2} = 22$  GPa and 30 GPa by means of nuclear resonant scattering<sup>9</sup> and synchrotron radiation Mössbauer spectroscopy,<sup>13</sup> respectively. Co metal undergoes two-step hydrogenation at high temperatures.<sup>14</sup> Above 250 °C, Co is hydrogenated to hcp-CoH $_x$  with  $x \approx 0.6$  up to  $p_{H_2} = 7$  GPa, and then exhibits the second transformation to fcc-CoH $_x$  with  $x \approx 1.0$ . Both phases are considered to be ferromagnetic. Hydrogenation to NiH is observed at a lower pressure ( $p_{H_2} \approx 0.8$  GPa) than those of Fe and Co. NiH forms the fcc structure. It is reported that magnetization of NiH $_x$  decreases with increasing  $x$ , and, reaches zero at  $x \approx 0.6$ .<sup>15</sup> The paramagnetic state of NiH is confirmed down to 4.2 K.<sup>6</sup>

The collapse of ferromagnetism in NiH suggests that hydrogenation significantly suppresses magnetization of TM. CoH also has smaller magnetization than Co; a decrease at a rate of  $-0.36 \mu_B/x$  was reported.<sup>16</sup> In FeH, Mössbauer spectroscopy by Choe *et al.* revealed two different hyperfine fields corresponding to the  $2a$  and  $2c$  sites of Fe,<sup>8</sup> and they reported that both were smaller than the hyperfine field of bcc-Fe. Thus, occupation by hydrogen seems to weaken the spin polarization of the TM  $3d$  orbital. It is interpreted by that  $3d$  density of states (DOS) is more occupied due to hydrogenation if we assume an unchanged profile of the  $3d$  DOS. This model is the so-called "rigid  $d$ -band model" and has succeeded in semiquantitatively elucidating the magnetization of the TM hydrides.<sup>17</sup> This interpretation well demonstrates that both theoretical and experimental studies are indispensable to illustrate the reconstruction of the electronic structure around  $E_F$ . To our knowledge, many

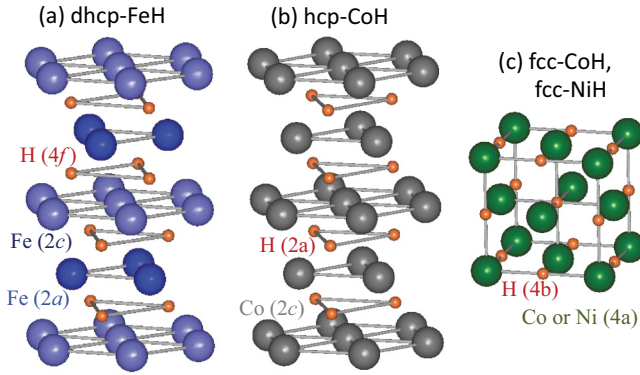


FIG. 1. (Color online) Crystal structures of (a) dhcp-FeH ( $P6_3/mmc$ ), (b) hcp-CoH ( $P6_3/mmc$ ), (c) fcc-CoH and NiH ( $Fm\bar{3}m$ ). Each atomic position is indicated by the Wyckoff position.

groups have already calculated DOS of the TM hydrides,<sup>18–23</sup> and they have carefully discussed hydrogen-induced changes in the electronic structure. However, experimental works under high pressure have been limited for the publications such as Mössbauer spectroscopy of FeH<sup>8,9,13</sup> and the metastable hydrides of Fe-based alloys at low temperatures.<sup>17</sup> The latter hydrides were measured at ambient pressure after being cooled under high pressure to liquid nitrogen temperature.<sup>17</sup>

Here, we have discussed hydrogen-induced modification of the electronic structures, magnetic states, and crystal structures of TM (=Fe, Co, and Ni) hydrides by three methods: x-ray magnetic circular dichroism (XMCD) at the TM  $K$ -edge, x-ray diffraction, and first-principles calculation. XMCD at the  $K$ -edge is a spectroscopic technique that probes magnetically polarized electronic states even under high pressure.<sup>24,25</sup> As far as the experiment under high pressure, it is unfeasible to measure XMCD at the TM  $L$ -edges located in the soft x-ray region because of the tremendous x-ray absorption by a pressure cell. The  $1s \rightarrow 4p$  dipole transition is dominant at the  $K$ -edge, however, XMCD originates not only from  $4p$  magnetic states but also from  $3d$  magnetic states via  $4p$ - $3d$  hybridization with neighboring atoms.<sup>26</sup> This study demonstrates that XMCD at the  $K$ -edge is capable of probing  $3d$  magnetic states in the TM hydrides. The crystal structures of Co and Ni hydrides were determined using the x-ray diffraction technique; the hydrogenation processes and compressibility among the TM hydrides were compared. The DOS of TM hydrides was evaluated by the first-principles calculation. Reconstruction of the electronic structure due to hydrogenation, the hydrogen effect on the magnetic state, and the stability of the ferromagnetic state under pressure have been investigated from both experimental and theoretical viewpoints.

## II. EXPERIMENTAL PROCEDURE

Polycrystalline metal foils (3–5  $\mu\text{m}$  thick) were prepared as a starting material. Diamond anvil cells (DAC) were employed to synthesize TM hydrides under pressure, and were used for the high-pressure experiments using synchrotron radiation. The sample was loaded into a hole of a tungsten gasket together with  $\text{H}_2$  fluid that was initially pressurized to 0.18 GPa. A versatile gas-loading system was utilized for  $\text{H}_2$  fluid loading.<sup>27</sup> The  $\text{H}_2$  fluid functioned as a pressure-transmitting

medium and as the source of hydrogen. A pair of small diamond anvils of 2.0 mm total thickness was adopted. The thin anvil effectively reduces x-ray absorption itself. The culet diameter of the anvils was 0.45 mm for Fe and Co, and 1.0 mm for Ni. The large culet for Ni is useful for adjusting pressures less than 1 GPa. The pressure applied to the sample was measured by the conventional ruby fluorescence method.<sup>28</sup>

X-ray absorption near edge structure (XANES) and XMCD measurements were carried out under high pressure on the beamline 39XU at SPring-8.<sup>29</sup> The incident x-ray beam was focused by a Kirkpatrick and Baez mirror,<sup>30</sup> and set to a size of  $7 \times 7 \mu\text{m}^2$  at the sample position. The XMCD spectra were measured by the helicity-modulation method.<sup>29</sup> A 0.45 mm thick diamond phase retarder was employed to produce x-ray beams with a high degree of circular polarization,  $P_c \geq 0.9$ .<sup>29</sup> A magnetic field of 0.6 T was applied parallel to both the incident x-ray beam and surface normal of the sample. XRD patterns of  $\text{CoH}_x$  and  $\text{NiH}_x$  were recorded at various pressures using the beamline BL04B2 at SPring-8 and BL-8B at Photon Factory. Imaging plates were available for data acquisition at both beamlines. All the measurements were done at RT.

The DOS of the TM hydrides, XANES, and XMCD were calculated using first-principles calculations based on density functional theory with the all-electron full-potential linear augmented plane wave (FLAPW) method.<sup>23</sup> Exchange and correlation were treated within its spin-polarized form with generalized gradient approximation (GGA). Uniform  $k$ -mesh sets of  $50 \times 50 \times 30$  for Co,  $50 \times 50 \times 50$  for Ni,  $40 \times 40 \times 10$  for FeH, and  $40 \times 40 \times 40$  for other samples were used for integration in the Brillouin zone. The muffin-tin sphere radii were set to 1.0  $\text{\AA}$  for TM and 0.59  $\text{\AA}$  for H. Plane-wave cutoffs were 20 and 200 Ry for the LAPW basis functions and the potential and charge density, respectively. To simulate XANES, and XMCD spectra, the probability of transition per unit time was given by the Fermi's golden rule and the transition matrix elements were calculated taking into account the electric dipole transitions.

## III. RESULTS AND DISCUSSION

### A. Synthesis and crystal structure of TM hydrides under high pressure

Figure 2 shows the molar volume  $V$  of Co, Ni, and their hydrides as a function of  $p_{\text{H}_2}$  at RT. These hydrogenation processes were determined by XRD patterns that were recorded using an imaging plate. Figure 3 displays typical XRD patterns of Co and Ni together with fitted curves at selected pressures. XRD patterns of FeH were not taken in our study, as they have already been studied elsewhere.<sup>11,31</sup> We used XANES and XMCD techniques to study the hydrogenation process of Fe.<sup>10</sup> Hydrogenation to FeH occurred in a narrow pressure range between 3.2 and 3.8 GPa. To evaluate the hydrogen content  $x$ , we refer to the linear relationship between  $V$  and  $x$ ,  $dV/dx \approx 2 \text{\AA}^3$ , which is reported by Fedotov *et al.*<sup>32</sup> In this study, the volume expansion of each sample reaches about  $2 \text{\AA}^3$ , indicating that  $x \approx 1$  is achieved at the end of the hydrogenation. TM hydrides undergo 16–20% volume expansion with respect to  $V$  of pure metals at the corresponding pressure.

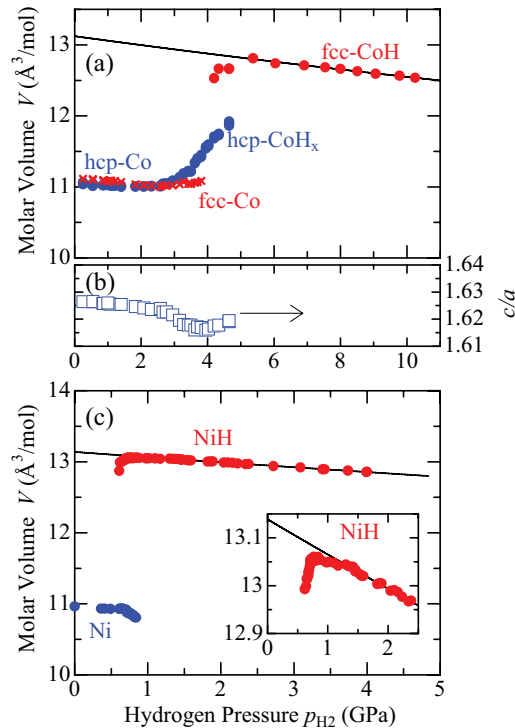


FIG. 2. (Color online) Molar volume  $V$  and  $c/a$  ratio as a function of hydrogen pressure  $p_{\text{H}_2}$ : (a)  $V$  of Co and CoH, (b)  $c/a$  ratio in hcp-CoH $_x$ , and (c)  $V$  of Ni and NiH. Solid lines denote curves fitted by the Birch-Murnaghan equation of states. The crosses in panel (a) denote  $V$  of the fcc-Co minor phase. The inset of panel (c) illustrates an enlarged plot of  $V$  at the lower pressure region of NiH.

Co exhibits two-step hydrogenation at RT as well as experiments at high temperatures.<sup>14</sup> Figure 3(a) shows that the starting material contains a small portion of fcc-Co, however, this minor phase disappears at  $p_{\text{H}_2} = 3.7\text{--}3.8$  GPa. The  $V$  of the hcp-Co majority phase is gradually expanded against increasing  $p_{\text{H}_2}$ , demonstrating that Co is hydrogenated above

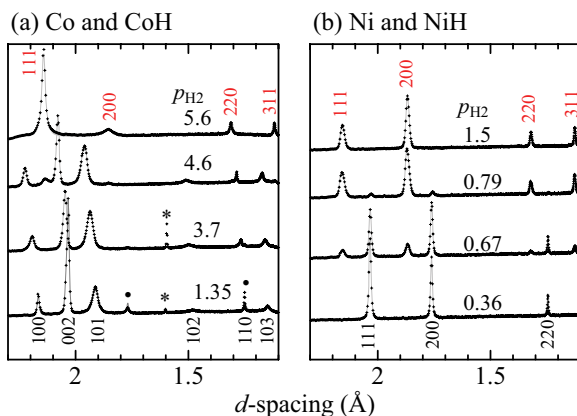


FIG. 3. (Color online) X-ray diffraction patterns of (a) Co and (b) Ni and their hydrides at selected pressures. Solid gray lines denote fitted curves of x-ray diffraction patterns by using RIETAN 2000 program.<sup>34</sup> Indices shown at bottom and top of the panels correspond to  $hkl$  reflection from TM and TM hydride, respectively. The dots in panel (a) indicate 200 and 220 reflections from the fcc-Co minor phase. Asterisks indicate diffraction from ruby chips.

$p_{\text{H}_2} = 2.7$  GPa but maintains the hcp structure. Hydrogen content in hcp-CoH $_x$  increases up to  $x \approx 0.6$ . At  $p_{\text{H}_2} \geq 4.2$  GPa, new reflections appear. This means that hcp-CoH $_{0.6}$  partially transforms to fcc-CoH $_x$  accompanied by volume expansion. The hydrogen content in the fcc-CoH $_x$  is estimated to be  $x \approx 0.9$ . Figure 2(b) shows that the  $c/a$  ratio significantly decreases at  $p_{\text{H}_2} \approx 2.7$  GPa and increases at  $p_{\text{H}_2} \approx 4$  GPa. These pressure dependences of  $c/a$  ratio correspond well to the hydrogenation to hcp-CoH $_x$  and the sudden appearance of fcc-CoH $_{0.9}$ , respectively. After the small volume expansion of fcc-CoH $_x$  in the coexistence region, monohydride (fcc-CoH) is synthesized and this phase exists as a single phase above  $p_{\text{H}_2} \approx 5$  GPa. The pressure-volume relation of fcc-CoH is well described by the Birch-Murnaghan equation of states (B-M EOS),<sup>33</sup> suggesting that the hydrogen content no longer increases above 5 GPa.

In the earlier works at 325 °C, fcc-CoH $_x$  with an intermediate value of volume expansion was observed in the pressure interval 4.5–5.5 GPa, which has been regarded as a supercritical anomaly on the isotherm of hydrogen solubility in the fcc-Co.<sup>14</sup> As shown in Fig. 2(a), only the very small volume expansion of the fcc-CoH $_x$  minor phase is observed in the present study. This means that hydrogen content in the minor phase is less than 0.1 at  $p_{\text{H}_2} \leq 3.7\text{--}3.8$  GPa; we conclude that fcc-CoH $_x$  with the moderate hydrogen content ( $x \approx 0.5$ ) is not confirmed at RT. Thus the region of the metastable isomorphous transformation between the H-depleted and H-rich hydride phases of the solid fcc-Co–H solutions probably terminates at a critical point somewhere between 325 °C and RT. This suggests that CoH $_x$  with hcp structure is rather stable at  $p_{\text{H}_2} \leq 5$  GPa at RT. We also note that the transformation pressure  $p_{\text{H}_2} \approx 5$  GPa to fcc-CoH at RT is remarkably lower than the value extrapolated from the reported  $p_{\text{H}_2}$ – $T$  hydrogen solubility diagram,<sup>5,6,14</sup> the transformation to fcc-CoH under high temperatures has been observed at  $p_{\text{H}_2} = 7$  GPa. Therefore, phase boundaries to fcc-CoH with a positive slope would be depicted in the  $p_{\text{H}_2}$ – $T$  phase diagram.

Figure 2(c) shows that Ni monohydride abruptly appears accompanied with the huge jump of the molar volume  $\delta V \approx 2 \text{ \AA}^3$ , which is in contrast to the two-step hydrogenation of Co. The XRD patterns show that Ni atoms still form an fcc structure in NiH. The coexistence of Ni and NiH is observed in a narrow pressure range,  $0.67 \text{ GPa} \leq p_{\text{H}_2} \leq 0.86 \text{ GPa}$ . The inset in Fig. 2(c) shows that NiH deviates from the fitted B-M EOS in the low pressure region. Hence,  $V$  of NiH slightly changes even above the coexistence region, suggesting that the hydrogen content  $x$  does not reach 1.0 at 0.86 GPa and gradually increases to  $\sim 1.0$  in the pressure range 0.86–1.4 GPa. The additional increase in  $x$  is estimated to be  $x \approx 0.02$ . The intermediate phase NiH $_{0.6}$  that was reported in Ref. 15 was not synthesized in our study.

The bulk modulus  $B_0$  is estimated from the fitting of B-M EOS. The result is summarized in Table I. The pressure derivative of the bulk modulus  $B'_0$  of Co and Ni hydrides is fixed to four because compressibility data is available in a limited pressure range. We note that the  $B_0$  of CoH is comparable to that of Co, while FeH has smaller  $B_0$  than both bcc and hcp phases of pure metals.  $B_0$  of NiH exhibits a moderate reduction. This difference is associated with the magnetic states of TM hydrides, as discussed in the last paragraph of subsection D.

TABLE I. Bulk modulus  $B_0$ , the pressure derivative of bulk modulus  $B'_0$ , and molar volume at ambient pressure  $V_0$  evaluated by fitting B-M EOS.

	Crystal structure	$B_0$ (GPa)	$B'_0$	$V_0$ ( $\text{\AA}^3$ )
Fe	bcc	166(7) <sup>a</sup>	4(fix)	11.73(1)
Fe	hcp	164.8(3.6) <sup>b</sup>	5.33	11.18(2)
FeH	dhcp	147(6) <sup>c</sup>	4(fix)	13.88(5)
Co	hcp	199 <sup>d</sup>	3.6	11.08
CoH	fcc	204(9)	4(fix)	13.12(3)
Ni	fcc	181 <sup>d</sup>	5.2	10.96(2)
NiH	fcc	176(2)	4(fix)	13.14(2)

<sup>a</sup>References 35 and 36.

<sup>b</sup>Reference 37.

<sup>c</sup>Reference 31.

<sup>d</sup>Reference 38.

### B. Density of states (DOS) of TM hydrides

Figure 4 shows DOS of TM hydrides together with those of pure metals. To examine the influence of hydrogen occupancy on the electronic structure, we calculated the DOS of the hydrides and starting metals with the same crystal structures of the metal lattices. The lattice parameters of TM hydrides and fcc-Co were determined from the calculated equilibrium volume. The structural parameters of other samples were evaluated from the XRD patterns at ambient pressure. The structural parameters used are summarized in Table II. For a useful comparison, insets of Fig. 4 show DOS of the TMs with the crystal structures experimentally observed: bcc-Fe and hcp-Co. Figure 5 displays the partial DOS of each orbital with majority spin in Ni and NiH. The partial DOS with minority spin is not shown because the shapes of the DOS are very similar to those for the majority spin except for the position of  $E_F$ . As mentioned above, the DOS of each hydride was carefully investigated and already published elsewhere.<sup>19–23</sup> Our calculation well reproduces the results of the earlier theoretical works. In Figs. 4 and 5, the sharp peaks around  $E_F$  mainly consist of 3d band structure originating from overlap between TM 3d orbitals of neighboring sites. The spin polarization of dhcp-Fe is absent, so that the paramagnetic phase is a ground state for the calculated equilibrium volume. On the other hand, bcc-Fe is ferromagnetic, and its electronic structure with spin polarization is classified as weak ferromagnetism (WF), where both majority and minority 3d band are partially occupied.<sup>39</sup> Co and Ni have electronic structures classified as strong ferromagnetism (SF), where the majority 3d band is fully occupied, and the minority band has unoccupied states.<sup>39</sup> The profiles of DOS for fcc-Co is nearly the same as that for hcp-Co, so that the electronic structures of the two phases are almost identical.

Three changes are observed in the DOS after hydrogenation: (i) the appearance of bonding and antibonding states below and above the 3d band. These states consist of hybridization between TM 4s, 4p, 3d, and H 1s electrons, and are located at around  $E_F - 7$  eV and  $E_F + 4$  eV, respectively. (ii) Narrowing of the 3d band. This is caused by reduced overlap between TM 3d orbitals due to hydrogen-induced volume expansion. The lower energy region of the 3d band decreases considerably due to hydrogenation, whereas the

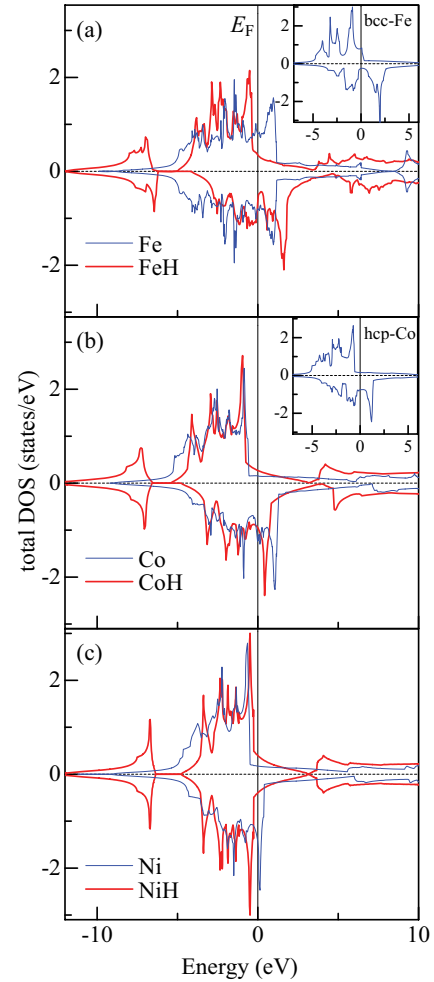


FIG. 4. (Color online) Total DOS (thick lines) of (a) dhcp-FeH, (b) fcc-CoH, and (c) fcc-NiH together with DOS of pure metals with the same crystal structure (thin lines). For dhcp-FeH, the Wyckoff position of hydrogen atom is set to  $4f(1/3, 1/3, z)$  and  $z = 0.880$ . The vertical line indicates the Fermi energy  $E_F$ . The insets in panel (a) and (b) represent the total DOS of bcc-Fe and hcp-Co, respectively.

profile of the upper region remains practically unaltered if the symmetry of the crystal structure of the TM is not changed.<sup>17,19</sup> (iii) Significant shift of the 3d band with respect to the  $E_F$ . Consequently, the 3d band with minority spin is more occupied in the case of CoH and NiH. The paramagnetic dhcp-Fe transforms to ferromagnetic FeH. Compared with the 3d band of dhcp-Fe, the 3d band of FeH with majority spin is mostly occupied whereas the band with minority spin moves upward as a result of the spin polarization. Therefore, the electronic structure of FeH is classified as SF, which is similar to the SF for CoH and is different from the WF for ferromagnetic bcc-Fe. In Fig. 4(c), the 3d band of NiH moves below  $E_F$ ; both majority and minority Ni 3d band are mostly occupied. Thus the calculation indicates that the spin polarization vanishes, and NiH is no longer ferromagnetic.

As for CoH and NiH, hydrogenation reduces TM 3d spin magnetic moment ( $M_s$ ). In this study, the numbers of TM 3d electrons ( $N_{3d}$ ) with majority and minority spins are separately evaluated by the integration of 3d electrons in the muffin-tin spheres, and  $M_s$  is determined from the difference

TABLE II. Lattice parameters used for the first-principles calculation and the spin magnetic moment of  $3d$  orbital ( $M_s$ ).  $\delta N_{3d}$  is the difference in the number of  $3d$  electrons  $N_{3d}$  between TM and TM hydrides.  $\delta N_{3d}$  is obtained by subtracting the  $N_{3d}$  of TM from that of TM hydrides. The calculated equilibrium volume was used for the lattice parameters of TM hydrides and fcc-Co. The structural parameters of other TMs are evaluated from the XRD patterns at 0 GPa.

		$a$ (Å)	$c$ (Å)	$M_s$ ( $\mu_B$ )	$\delta N_{3d}$
Fe	bcc	2.866		2.26	
Fe	dhcp	2.439	7.888	0.0	
FeH	dhcp	2.645	8.669	1.91 (Fe 2a)	0.094 <sup>a</sup>
				2.09 (Fe 2c)	0.086 <sup>a</sup>
Co	hcp	2.508	4.089	1.72	
Co	fcc	3.524		1.71	
CoH	fcc	3.701		1.25	0.111 <sup>b</sup>
Ni	fcc	3.526		0.69	
NiH	fcc	3.721		0.0	0.118

<sup>a</sup>TM = bcc-Fe. In the case of TM = dhcp-Fe,  $\delta N_{3d}$  is evaluated to be 0.066 for Fe(2a) and 0.058 for Fe(2c).

<sup>b</sup>TM = hcp-Co. In the case of TM = fcc-Co,  $\delta N_{3d}$  is evaluated to be 0.102.

of  $N_{3d}$  between different spins. The calculated values of  $M_s$  in Table II are in good agreement with the experimentally reported values.<sup>15–17</sup>  $M_s = 0.69 \mu_B$  of Ni vanishes when paramagnetic NiH is synthesized. The decrease in  $M_s$  of Co is evaluated to be  $0.47 \mu_B$ , and the decrease does not depend on the starting crystal structures of Co: fcc and hcp. According to the rigid  $d$ -band model,<sup>17</sup> the reduced  $M_s$  is attributed to the additional filling in the  $3d$  minority band, because the  $3d$  majority band is mostly occupied and less effective to the magnetic properties. The hydrogen-induced change in  $M_s$  is dissimilar in the case of FeH. The earlier experimental

study<sup>17,40</sup> and our calculation reveal that  $M_s$  of dhcp-FeH is comparable with or slightly smaller than that of bcc-Fe. If we assume that the crystal structure of the Fe atoms does not change by hydrogenation, the transition from paramagnetic dhcp-Fe to ferromagnetic dhcp-FeH results in the opposite sign of the effect of hydrogen on  $M_s$ : hydrogen increases  $M_s$  from zero to  $\sim 2\mu_B$  at Fe 2a and 2c sites.

In contrast to the drastic changes in  $M_s$  and the  $3d$  band,  $N_{3d}$  of the hydrides is almost unchanged by hydrogenation.<sup>21</sup> As shown in Table II, the hydrogenation-induced increase in  $N_{3d}$  ( $\delta N_{3d}$ ) is estimated to be  $\sim 0.1$  electrons or less even though the additional filling to the  $3d$  band occurs in the case of CoH and NiH. The small  $\delta N_{3d}$  indicates that substantial numbers of unoccupied  $3d$  states are reserved above  $E_F$  of the TM hydrides. Compared to the electronic structure in TMs, that in the TM hydrides possesses high densities just above  $E_F$ , where the unoccupied minority  $3d$  band and the antibonding states are located. The partial DOS shown in Fig. 5 demonstrates that meaningful unoccupied  $3d$  component is reserved in the antibonding state. The  $3d$  states in the antibonding state are important to elucidate the characteristic XMCD profile of the TM hydrides.

With regard to the charge reconstruction upon hydrogenation, the electron density around the H atom in a metal hydride is always noticeably higher than that around the isolated H atom. This reconstruction is recently carefully depicted in a paper by Smithson *et al.*<sup>18</sup> The attractive electrostatic potential of the proton causes the bonding state with two electrons, and the charge density is spherically distributed ( $s$ -character) around the proton.<sup>19,20</sup> The extra electrons needed to increase charge come from the interstitial charge density that is mainly distributed outside of the muffin-tin spheres. We consider that the electron charge mainly moves from TM  $sp$  conduction electrons to hydrogen  $1s$  electrons. Therefore, the antibonding state is dominated by the TM  $3d$  and  $sp$  components while its bonding counterpart has a large H  $1s$  component.

### C. Electronic and magnetic states of TM hydrides determined by XANES and XMCD

Figure 6 shows XANES and XMCD profiles of TMs and TM hydrides. Hydrogenation modifies both XMCD and XANES spectra. For XANES of TMs, shoulder structure **a** is commonly observed near the absorption edge  $E_0$ . A different profile at the absorption maximum **b** originates from the crystal structure; i.e., bcc for Fe, hcp for Co, and fcc for Ni. TM hydrides exhibit a suppressed shoulder **a'** and a crest **b'**. These characteristics are observed in all the TM hydrides. The common profile means that the  $4p$  unoccupied state is almost the same in the hydrides, even though the crystal structure of FeH (dhcp) is different from the fcc structures of CoH and NiH.

The chemical shift of  $E_0$  is useful for investigating the valence state of TM atoms. In this study,  $E_0$  was determined from the first inflection point near the shoulders **a** and **a'**.  $E_0$  moves to lower energies after hydrogenation, however, the shift ranges between 0.2 and 0.3 eV. Hence, TM remains neutral or is slightly electronegative after hydrogenation, suggesting that the TM hydrides are not ionic but metallic. This is consistent with the theoretical investigation of the small  $\delta N_{3d}$  within 0.1 electrons.

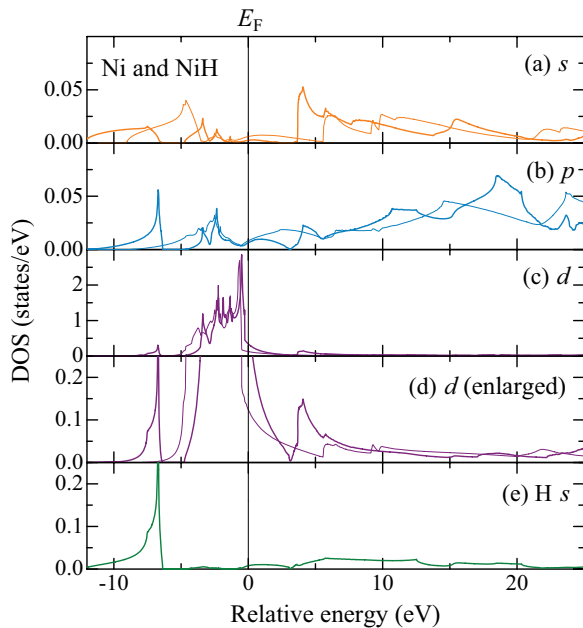


FIG. 5. (Color online) Partial DOS of Ni- $s$ ,  $p$ ,  $d$ , and H- $s$  orbitals with up-spins in Ni (thin lines) and NiH (thick lines). The panel (d) shows an enlarged figure of the Ni- $d$  orbital.

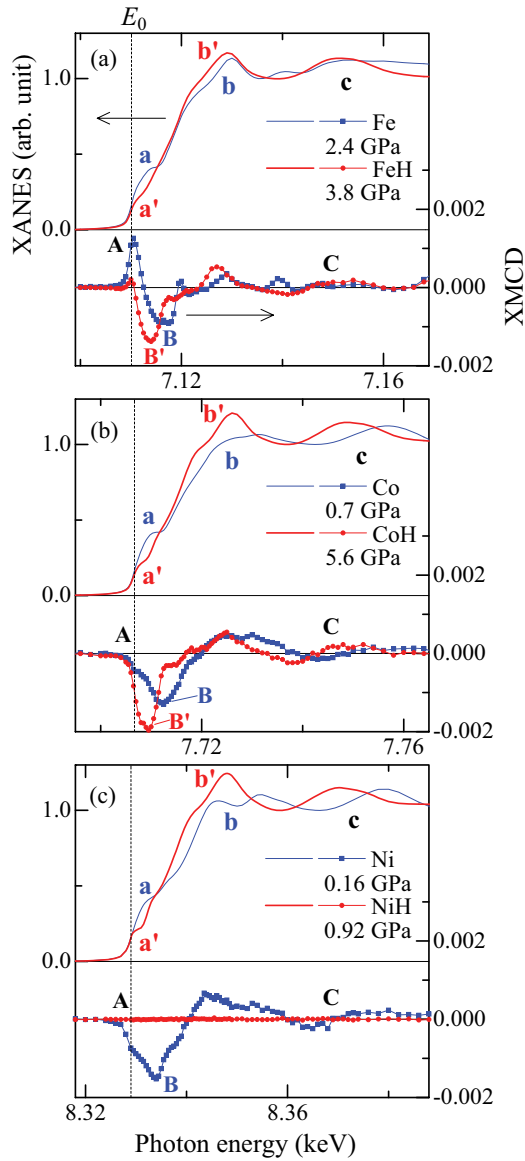


FIG. 6. (Color online) XANES and XMCD spectra of TM and their hydrides: (a) Fe, (b) Co, (c) Ni. The vertical broken lines indicate the absorption edge  $E_0$ .

The XMCD of bcc-Fe shows a dispersion-type profile that consists of a positive peak **A** and a negative peak **B**. XMCD spectra of Co and Ni are characterized by the large negative peak **B** without the positive peak **A**. The XMCD spectra of both FeH and CoH have the sharp negative peak **B'**, and only FeH shows a small positive peak **A** near  $E_0$ . The remaining XMCD demonstrates that FeH and CoH preserve ferromagnetic states. On the other hand, the XMCD spectrum of NiH vanishes, so that the magnetic state of NiH is paramagnetic, as reported in previous studies.<sup>6,15</sup>

XANES and XMCD spectra exhibit oscillating profiles referred to as **c** and **C** in the higher energy range. Both profiles move to the lower energy direction after hydrogenation. Since these spectra are classified as EXAFS and magnetic EXAFS, respectively, the shifts are attributed to structural origin mainly due to volume expansion. To distinguish modifications by volume expansion and those by electronic structure, the spectra

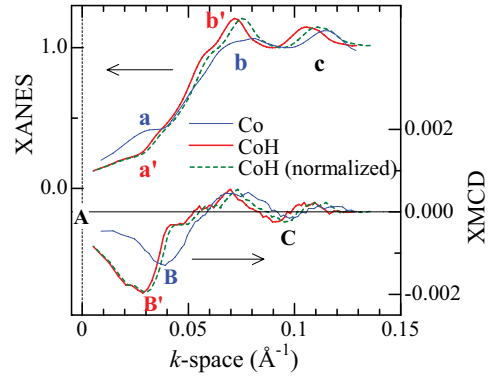


FIG. 7. (Color online) XANES and XMCD spectra of Co and CoH as a function of reciprocal space  $k$ . The broken lines represent normalized XANES and XMCD profiles of CoH with assumption of the same unit cell volume of Co.

of Co and CoH are plotted as a function of  $k$ -space, as shown in Fig. 7. The broken lines represent normalized XANES and XMCD spectra of CoH, where  $k$  is multiplied by the factor 1.049 that corresponds to the  $V^{-3}$  ratio of CoH to Co. This normalization yields a spectrum of CoH without volume expansion. For the normalized XANES, the peak in the range **c** moves toward the corresponding peak of Co, so that the oscillating profile above  $k \approx 0.1 \text{ \AA}^{-1}$  is caused by volume expansion. In the case of XMCD, the influence of volume expansion is recognized in the shift of the oscillating profile **C** at  $k \geq 0.06 \text{ \AA}^{-1}$ . The normalized profiles show a similar oscillation frequency for Co, whereas the profile around  $E_0$  clearly differs from that of Co. Therefore, the XANES profiles of **a**–**b'** and XMCD of **A**–**B'** originate from the electronic structure.

In the case of XMCD, the electronic structure's contribution is observed in the narrow region around  $E_0$ . This result is interpreted by the considerable influence from the electronic structure of TM  $3d$  orbital near  $E_F$ . The sensitivity of the  $K$ -edge XMCD to the  $3d$  states is mediated by  $4p$ - $3d$  hybridization with neighboring TM atoms. Igarashi and Hirai have theoretically explained the XMCD profiles of Fe, Co, and Ni: Suppression of the positive peak **A** occurs with increasing valence electrons,<sup>41</sup> and the XMCD profile strongly depends on TM  $3d$  orbital moment density.<sup>26,41</sup> To examine this trend experimentally, we paid attention to the XMCD profile around  $E_0$ . Figure 6 shows that peak **A** disappears, and the sign of the intensity at  $E_0$  changes from positive to negative with the replacement Fe  $\rightarrow$  Co. The XMCD profile of Ni has a more negative component at  $E_0$ , indicating that the negative component of the XMCD intensity at  $E_0$  increases as  $N_{3d}$  increases. However, the change at Co  $\rightarrow$  Ni is very small in contrast to the drastic change at Fe  $\rightarrow$  Co. This trend suggests a strong contribution of the classification of the TM  $3d$  electronic structure, i.e., WF for Fe and SF for both Co and Ni. Hence, the sudden disappearance of peak **A** is mainly attributed to the changes from WF to SF accompanied by the small effect from the increasing  $N_{3d}$ .

This relationship can be employed to investigate the modification of  $3d$  states in the hydrides. The positive peak **A** is abruptly suppressed during hydrogenation to FeH, and the peak **A** intensity of FeH can be plotted between the values of Fe and Co. The small peak **A** suggests that the electronic structure of FeH approaches SF from WF, as predicted by the calculated

DOS [see Fig. 4(a)]. The XMCD of CoH has a negative peak **B'**, and the positive peak **A** is absent as well as the XMCD of Co, indicating that the electronic structure of CoH is also classified as SF. As shown in Fig. 6, the XMCD intensity of CoH at  $E_0$  is slightly larger than the magnitude of Co, implying the small positive  $\delta N_{3d}$  at the end of hydrogenation.

For FeH and CoH, the negative peak **B'** shifts towards  $E_0$  and exhibits a profile with large amplitude and a narrow width of  $\sim 7$  eV. This narrow width means that a large  $3d$  orbital moment density exists just above  $E_F$ , which also indicates that the unoccupied  $3d$  states with spin and orbital polarization concentrate near  $E_F$ . According to the total and partial DOS, the unoccupied  $3d$  band with minority spin and antibonding state are located in the corresponding energy range up to  $\sim E_F + 7$  eV. Therefore, enhancement of  $3d$  orbital moment in these hydrogen-induced electronic structures is probably responsible for the sharp XMCD profile. This result also suggests that the antibonding state has a substantial  $3d$  component.

The suppression of shoulder **a** to **a'** is also related to the appearance of the antibonding state. Shoulder **a** is attributed to  $p$ - $d$  hybridization with neighboring TM atoms.<sup>42</sup> When hydrogen atoms occupy the interstitial sites of the TM lattices, the antibonding state due to hybridization with the H  $1s$  orbital appears whereas the  $p$ - $d$  hybridization diminishes. Consequently, hydrogenation reduces TM  $4p$  unoccupied DOS near  $E_F$  and increases  $3d$  DOS in this region. The XANES profile shows that hydrogenation pushes TM  $4p$  DOS up to higher energies, which is clearly recognized by the enhancement of the crest **b'**. The partial DOS of the Ni  $4p$ -orbital, shown in Fig. 5(b), reproduces this modification: The decrease and the enhancement of the TM  $4p$  DOS are recognized at around  $E_F + 3$  eV and  $E_F + 18$  eV, respectively. These energies are almost similar to the positions of **a'** and **b'**. The common characteristics of the XANES profiles reveal that FeH, CoH, and NiH undergo similar modifications of the  $4p$  electronic states due to the appearance of the antibonding state.

The calculated XANES and XMCD spectra of the TM hydrides are shown in Fig. 8. The calculated XANES spectra are in fair agreement with the experimental data, e.g.,

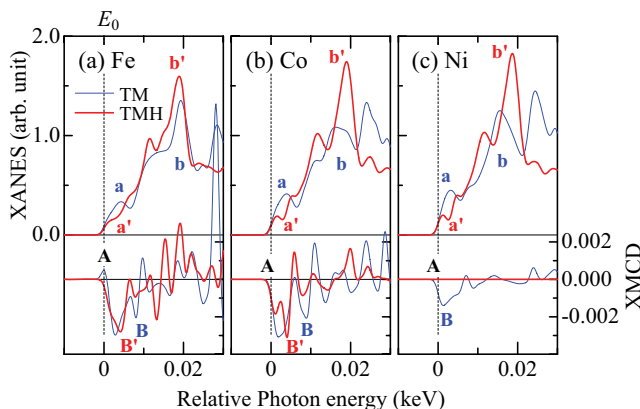


FIG. 8. (Color online) Calculated XANES (upper part) and XMCD spectra (lower part) of TMs (thin lines) and TM hydrides (thick lines): (a) Fe, (b) Co, (c) Ni. The average profiles of the two spectra originating from the Fe(2a) and Fe(2c) sites is shown for FeH.

suppression of shoulder **a** to **a'**, enhancement of crest **b** to **b'**. This consistency supports our interpretation of the electronic structure discussed above. On the other hand, the calculated XMCD demonstrates the difficulty of taking the spin and orbital polarized states of the spatially extended TM  $p$ -state into account. In particular, the oscillating structure of XMCD at higher energies than  $E_0$  is more enhanced than the experimental data, and the intensity of the positive peak **A** of Fe seems underestimated. However, the calculation qualitatively reproduces the increase in the negative component of peak **A** accompanying the change Fe  $\rightarrow$  FeH. This is probably related to the change of the electronic structure from WF to SF. We also note that the sharp profile of the calculated negative peak **B'** is in rough agreement with the experimental result.

#### D. Stability of the ferromagnetic states in TM hydrides

The stability of the ferromagnetic states in FeH and CoH is determined by the pressure dependence of XMCD. Figure 9 shows the integrated intensity of XMCD,  $I_{\text{mcd}}$ , as a function of  $p_{\text{H}_2}$ . In Fig. 9, the  $I_{\text{mcd}}$  of Ni metal<sup>24</sup> and of Co metal<sup>43</sup> are displayed for comparison.  $I_{\text{mcd}}$  is evaluated from the main part of the XMCD consisting of the peaks **A**–**B'**. The normalized slope of  $I_{\text{mcd}}$ , defined as

$$\zeta \equiv \frac{1}{I_{\text{mcd}}^0 \text{GPa}} \frac{d}{dp} I_{\text{mcd}}, \quad (1)$$

is used to compare the pressure dependence of XMCD.  $I_{\text{mcd}}^0 \text{GPa}$  corresponds to the value of  $I_{\text{mcd}}$  at ambient pressure. Each  $\zeta$  was evaluated by least squares fitting. The  $I_{\text{mcd}}^0 \text{GPa}$  of FeH and CoH were determined by the extrapolation of  $I_{\text{mcd}}$  to the ambient pressure.

A sharp increase in  $I_{\text{mcd}}$  is observed for Fe between  $p_{\text{H}_2} = 3.2$  and  $3.8$  GPa where hydrogenation to dhcp-FeH occurs. The  $I_{\text{mcd}}$  of FeH linearly decreases up to 20 GPa with a slope of  $\zeta = -1.3(2) \times 10^{-2} \text{GPa}^{-1}$ . Above 20 GPa, the slope becomes steep. At 27.5 GPa, the  $I_{\text{mcd}}$  is about 16% of that at 3.8 GPa. Extrapolating the decrease in  $I_{\text{mcd}}$ , we determine the critical

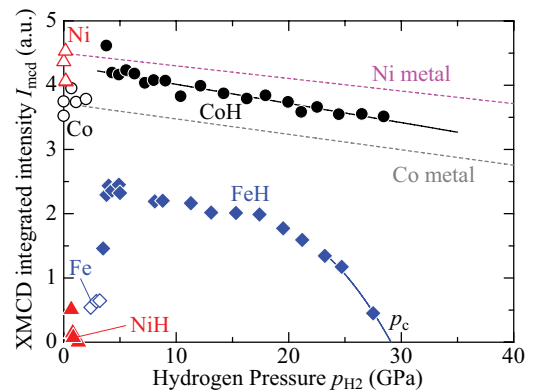


FIG. 9. (Color online) Integrated intensity  $I_{\text{mcd}}$  of XMCD for FeH (closed diamonds), CoH (closed circles), and NiH (closed triangles) as a function of  $p_{\text{H}_2}$ .  $I_{\text{mcd}}$  for pure metals is represented by open symbols. For comparison, the pressure dependence of Co metal and Ni metal using standard pressure transmitting medium is shown by the broken lines.<sup>24,43</sup>  $p_c$  represents an estimated critical pressure of ferromagnetic FeH.

pressure  $p_c$  to be  $\sim 29.5$  GPa, at which XMCD vanishes. Above  $p_c$ , FeH is paramagnetic and the Curie temperature  $T_C$  would be reduced to below RT. It is thought that  $p_c$  increases at low temperatures. According to the theoretical calculations,  $p_c$  is predicted to be 60 GPa in Ref. 44 and 48 GPa in Ref. 23 at 0 K.

An increase in  $I_{\text{mcd}}$  for CoH appears accompanied by hydrogenation to CoH up to about  $p_{\text{H}_2} = 5$  GPa. The  $I_{\text{mcd}}$  of CoH linearly decreases with a slope of  $\zeta = -6.9(5) \times 10^{-3} \text{ GPa}^{-1}$ . There are no sudden drops up to the maximum pressure of 29 GPa, which is in contrast to the pressure dependence of FeH. CoH has an absolute value of  $\zeta$  that is about two times smaller than that of FeH, indicating that ferromagnetic CoH is more stable. It is noted that the  $\zeta$  of CoH is comparable to those of Co and Ni, i.e.,  $\zeta = -6.5(2) \times 10^{-3} \text{ GPa}^{-1}$  for Co and  $\zeta = -4.4(3) \times 10^{-3} \text{ GPa}^{-1}$  for Ni. Because the ferromagnetic states of Co and Ni are preserved above 100 GPa,<sup>43,45</sup> this small pressure dependence demonstrates high stability of ferromagnetic CoH under pressure.

The appearance and the stability of ferromagnetic states can be understood on the basis of the Stoner criterion,  $1 \geq ID(E_F)$ , where  $I$  and  $D(E_F)$  denote the molecular field constant and DOS at  $E_F$ , respectively. The Stoner criterion suggests that a high  $D(E_F)$  is advantageous to the onset of a ferromagnetic transition. Volume expansion due to hydrogenation introduces a narrow  $3d$  band with high densities. Hydrogenation also causes the shift of  $E_F$  with respect to the  $3d$  band. Both phenomena provide a suitable condition to fulfill the Stoner criterion for ferromagnetic FeH and CoH. As shown in Fig. 4, on the other hand,  $E_F$  of paramagnetic NiH is located above the upper threshold of  $3d$  band because of the shift of  $E_F$ . Consequently, the  $D(E_F)$  of NiH is much smaller than those of FeH and CoH, and the Stoner criterion is unsatisfied for NiH.

Broadening of the  $3d$  band with increasing pressure is introduced by lattice contraction because of enhanced overlap between TM  $3d$  orbitals. This gives rise to a decrease in  $D(E_F)$ , and the ferromagnetic state is destabilized under high pressure. As for dhcp FeH, recent theoretical calculation has yielded the significant pressure-induced changes in the electronic structure: The largest peak in the DOS with majority spin, which appears at  $-0.5$  eV below  $E_F$  as shown in Fig. 4(a), broadens and moves to the energies above  $E_F$  under high pressure.<sup>23</sup> This causes small  $D(E_F)$ , and the Stoner criterion is hardly fulfilled. The remarkable difference of the stability between ferromagnetic FeH and CoH is probably attributed to different DOS profiles around  $E_F$ , because  $D(E_F)$  strongly depends on both the symmetry of the crystal structure and  $3d$  electron occupancy  $N_{3d}$ . The high stability of the ferromagnetic CoH infers that its  $D(E_F)$  is less influenced by the applied pressure.

Finally, we note that the stability of ferromagnetic states of FeH and CoH correlates well with  $B_0$ . As summarized in

Table I, FeH has a very small  $B_0$ , whereas  $B_0$  of CoH is large and is comparable to that of Co. In FeH, the small  $B_0$  indicates that the remarkable lattice contraction significantly modifies the electronic structure and destabilizes the ferromagnetic state. The strong correlation between the magnetic state and  $B_0$  of FeH is recognized by the fact that  $B_0$  increases again to 162(14) GPa above 30 GPa.<sup>31</sup> Hence,  $B_0$  becomes large when the ferromagnetic state disappears and paramagnetic FeH appears at  $p_c$ . Thus the magnetic state plays an important role in the cohesive properties. The less compressive behavior of CoH supports our speculation that the electronic structure of CoH is hardly influenced by the applied pressure.

#### IV. CONCLUSIONS

The electronic structures, magnetic states, and crystal structures of Fe, Co, and Ni hydrides were investigated by XMCD and XRD together with first-principles calculations, and the interactions with hydrogen and TM atoms were discussed. We revealed the different hydrogenation processes between CoH and NiH at RT. The XANES and XMCD are in fair agreement with the theoretical calculations, and successfully reveal the reconstruction of the electronic structure introduced by hydrogenation. In TM hydrides,  $E_F$  moves significantly with respect to the  $3d$  band; bonding and antibonding states appear below and above the  $3d$  band, respectively. The sharp XMCD profiles of FeH and CoH near  $E_0$  indicate that the orbital moment density of  $3d$  orbital is concentrated just above  $E_F$ , which is probably attributed to the hydrogen-induced electronic structure around  $E_F$ , i.e., the  $3d$  band with minority spin and the  $3d$  component in the antibonding states. The narrow  $3d$  band due to volume expansion and significant shift of  $E_F$  are responsible for the appearance of the ferromagnetism in FeH and CoH, whereas NiH is paramagnetic. The ferromagnetic state of FeH is less stable than that of CoH under pressure, indicating that  $3d$  DOS near  $E_F$  determines the magnetic state and its pressure dependence.

#### ACKNOWLEDGMENTS

We thank N. Hirao (JASRI/SPring-8), T. Mitsui, A. Machida (JAEA), and K. Aoki (Tohoku Univ.) for their fruitful discussion. This work was supported by grants from the NEDO project, ‘‘Advanced Fundamental Research on Hydrogen Storage Materials.’’ This work was partially supported by Grant-in-Aid for Young Scientists (B) (No. 23760670). The measurements were performed at SPring-8 with the approval of PRC-JASRI (Nos. 2008B1284, 2009B1011, 2010A1005, 2010B1520). This study was also approved by the Photon Factory Program Advisory Committee (Proposal No. 2009G659).

\*naoki@sci.hiroshima-u.ac.jp

<sup>1</sup>Y. Fukai, *The Metal-Hydrogen system*, 2nd ed. (Springer, Berlin, 2005).

<sup>2</sup>J. N. Huiberts, R. Griessen, J. H. Rector, R. J. Wijngaarden, J. P. Dekker, D. G. de Groot, and N. J. Koeman, *Nature (London)* **380**, 231 (1996).

<sup>3</sup>A. Fujita, S. Fujieda, Y. Hasegawa, and K. Fukamichi, *Phys. Rev. B* **67**, 104416 (2003).

<sup>4</sup>J. Chaboy and C. Piquet, *Phys. Rev. B* **66**, 104433 (2002).

<sup>5</sup>Y. Fukai, S. Yokota, and J. Yanagawa, *J. Alloys Compd.* **407**, 16 (2006).

<sup>6</sup>V. Antonov, *J. Alloys Compd.* **330-332**, 110 (2002).

- <sup>7</sup>V. Antonov, I. Belash, V. Degtyareva, E. Ponyatovskii, and V. Shiryayev, *Sov. Phys. Dokl.* **25**, 490 (1980).
- <sup>8</sup>I. Choe, R. Ingalls, J. M. Brown, Y. Sato-Sorensen, and R. Mills, *Phys. Rev. B* **44**, 1 (1991).
- <sup>9</sup>W. Mao, W. Sturhahn, D. Heinz, H. Mao, J. Shu, and R. Hemley, *Geophys. Res. Lett.* **31**, L15618 (2004).
- <sup>10</sup>N. Ishimatsu, Y. Matsushima, H. Maruyama, T. Tsumuraya, T. Oguchi, N. Kawamura, M. Mizumaki, T. Matsuoka, and K. Takemura, *Mater. Res. Soc. Symp. Proc.* **1262**, W04 (2010).
- <sup>11</sup>J. V. Badding, R. J. Hemley, and H. K. Mao, *Science* **253**, 421 (1991).
- <sup>12</sup>O. Mathon, F. Baudelet, J. P. Itié, A. Polian, M. d'Astuto, J. C. Chervin, and S. Pascarelli, *Phys. Rev. Lett.* **93**, 255503 (2004).
- <sup>13</sup>T. Mitsui and N. Hirao, *MRS Proc.* **1262**, W06 (2010).
- <sup>14</sup>V. E. Antonov, T. E. Antonova, M. Baier, G. Grosse, and F. E. Wagner, *J. Alloys Compd.* **239**, 198 (1996).
- <sup>15</sup>H. J. Bauer and E. Schmidbauer, *Z. Phys.* **164**, 367 (1961), in German.
- <sup>16</sup>I. Belash, V. Malyshev, B. Ponomarev, E. Ponyatovskii, and A. Sokolov, *Sov. Phys. Solid State* **28**, 741 (1986).
- <sup>17</sup>V. E. Antonov, M. Baier, B. Dorner, V. K. Fedotov, G. Grosse, A. I. Kolesnikov, E. G. Ponyatovsky, G. Schneider, and F. E. Wagner, *J. Phys.: Condens. Matter* **14**, 6427 (2002).
- <sup>18</sup>H. Smithson, C. A. Marianetti, D. Morgan, A. V. der Ven, A. Predith, and G. Ceder, *Phys. Rev. B* **66**, 144107 (2002).
- <sup>19</sup>P. Vargas and N. E. Christensen, *Phys. Rev. B* **35**, 1993 (1987).
- <sup>20</sup>C. Elsässer, J. Zhu, S. G. Louie, M. Fähnle, and C. T. Chan, *J. Phys.: Condens. Matter* **10**, 5081 (1998).
- <sup>21</sup>B. Szpunar, W. E. Wallace, and P. Strange, *J. Less-Common Metals* **123**, 37 (1986).
- <sup>22</sup>E. S. Alekseev, N. I. Kulikov, and A. F. Tatarchenko, *J. Less-Common Metals* **130**, 261 (1988).
- <sup>23</sup>T. Tsumuraya, Y. Matsuura, T. Shishidou, and T. Oguchi, *J. Phys. Soc. Jpn.* **81**, 064707 (2012).
- <sup>24</sup>N. Ishimatsu, H. Maruyama, N. Kawamura, M. Suzuki, Y. Ohishi, and O. Shimomura, *J. Phys. Soc. Jpn.* **76**, 064703 (2007).
- <sup>25</sup>V. Iota, J.-H. P. Klepeis, C.-S. Yoo, J. Lang, D. Haskel, and G. Srajer, *Appl. Phys. Lett.* **90**, 042505 (2007).
- <sup>26</sup>J.-i. Igarashi and K. Hirai, *Phys. Rev. B* **50**, 17820 (1994).
- <sup>27</sup>K. Takemura, P. C. Sahu, Y. Kunii, and Y. Toma, *Rev. Sci. Instrum.* **72**, 3873 (2001).
- <sup>28</sup>H. K. Mao, J. Xu, and P. M. Bell, *J. Geophys. Res.* **91**, 4673 (1986).
- <sup>29</sup>N. Kawamura, N. Ishimatsu, and H. Maruyama, *J. Synchrotron Rad.* **16**, 730 (2009).
- <sup>30</sup>H. Yumoto *et al.*, *Proc. SPIE* **7448**, 74480Z (2009).
- <sup>31</sup>N. Hirao, T. Kondo, E. Ohtani, K. Takemura, and T. Kikegawa, *Geophys. Res. Lett.* **31**, L06616 (2004).
- <sup>32</sup>V. K. Fedotov, V. E. Antonov, T. E. Antonova, E. L. Bokhenkov, B. Dorner, G. Grosse, and F. E. Wagner, *J. Alloys Compd.* **291**, 1 (1999).
- <sup>33</sup>F. Birch, *Phys. Rev.* **71**, 809 (1947).
- <sup>34</sup>F. Izumi and T. Ikeda, *Mater. Sci. Forum* **321-324**, 198 (2000).
- <sup>35</sup>D. R. Wilburn and W. A. Bassett, *Am. Mineral.* **63**, 591 (1978).
- <sup>36</sup>For bcc-Fe, many different values of  $B_0$  are reported because  $B_0$  strongly depends on  $B'_0$  value, hydrostatic conditions, and the bcc-hcp structural transition.
- <sup>37</sup>H. K. Mao, Y. Wu, L. C. Chen, J. F. Shu, and A. P. Jephcoat, *Geophys. Res.* **95**, 21737 (1990).
- <sup>38</sup>C. S. Yoo, H. Cynn, P. Söderlind, and V. Iota, *Phys. Rev. Lett.* **84**, 4132 (2000).
- <sup>39</sup>J. Stöhr and H. Siegmann, *Magnetism From Fundamentals to Nanoscale Dynamics* (Springer, Berlin, 2006), p. 524.
- <sup>40</sup> $M_s$  of the quenched metastable dhcp-FeH is  $2.2 \mu_B$  (Ref. 17). This value is nearly the same as that of bcc-Fe.
- <sup>41</sup>J.-i. Igarashi and K. Hirai, *Phys. Rev. B* **53**, 6442 (1996).
- <sup>42</sup>J. Chaboy, J. Garcia, and A. Marcelli, *J. Magn. Magn. Mater.* **166**, 149 (1997).
- <sup>43</sup>N. Ishimatsu, N. Kawamura, H. Maruyama, M. Mizumaki, T. Matsuoka, H. Yumoto, H. Ohashi, and M. Suzuki, *Phys. Rev. B* **83**, 180409 (2011).
- <sup>44</sup>C. Elsässer, J. Zhu, S. G. Louie, B. Meyer, M. Fähnle, and C. T. Chan, *J. Phys.: Condens. Matter* **10**, 5113 (1998).
- <sup>45</sup>R. Torchio, Y. O. Kvashnin, S. Pascarelli, O. Mathon, C. Marini, L. Genovese, P. Bruno, G. Garbarino, A. Dewaele, F. Occelli, and P. Loubeyre, *Phys. Rev. Lett.* **107**, 237202 (2011).